Arbitrary and Rigorous Aperture Illumination Synthesis in Huygens' Metasurface Metasurface Metasurface Metasurface Metasurface Metasurface Metasurface Metasurface Metasurface Metasurface Leaky-Wave Antennas

Pablo Mateos-Ruiz[1], Vinay Kumar Killamsetty[2], Ariel Epstein[2], and Elena Abdo-Sánchez [1]

[1]Telecommunication Research Institute (TELMA), University of Málaga, 29010 Málaga, Spain
[2]Andrew and Erna Viterbi Faculty of Electrical and Computer Engineering, Technion–Israel Institute of Technology, Haifa 32000, Israel

March 26, 2025

Abstract

Omega-type bianisotropic Huygens' Huygens' Huygens' Huygens' Huygens' Huygens' metasurfaces offer a novel approach approach approach approach approach approach for controlling the aperture field distribution of leaky-wave antennas. antennas. antennas. antennas. antennas. antennas. This paper presents a methodology utilizing a parallel-plate waveguide waveguide waveguide waveguide waveguide waveguide with a metasurface as its top plate. Previous limitations on constant constant constant constant constant constant leakage factor are addressed using a slowly varying amplitude amplitude amplitude amplitude amplitude amplitude approximation in order to satisfy Maxwell's Maxwell's Maxwell's Maxwell's Maxwell's Maxwell's wave equation, enabling the the the the the the design of the radiation pattern. A semi-analytical algorithm is employed employed employed employed employed employed to obtain the required multi-layer unit-cell geometries. Here, the the the the the the inter-layer coupling is taken into account, enabling an efficient efficient efficient efficient efficient efficient synthesis of these antennas. Several designs presenting different different different different different different pointing angles and aperture field distributions are carried out, out, out, out, out, out, showing very good agreement between theory and realistic simulations simulations simulations simulations simulations simulations without further full-wave optimization. Finally, the design process is is is is is experimentally validated through several prototypes, whose measurements measurements measurements measurements measurements measurements are shown and discussed. These results, demonstrating straightforward straightforward straightforward straightforward straightforward straightforward semi-analytical synthesis of versatile aperture profiles, would would would would would significantly broaden the applicability of such antennas in in in in in in next-generation wireless systems.systems.systems.systems.systems.systems.systems.systems.systems.systems.systems.systems.systems.systems.systems.systems.systems.system

Arbitrary and Rigorous Aperture Illumination Synthesis in Huygens Metasurface Leaky-Wave Antennas

Pablo Mateos-Ruiz, *Student Member, IEEE,* Vinay Kumar Killamsetty, *Student Member, IEEE,* Ariel Epstein, *Senior Member, IEEE,* and Elena Abdo-Sánchez, *Member, IEEE*

***Abstract*—Omega-type bianisotropic Huygens' metasurfaces offer a novel approach for controlling the aperture field distribution of leaky-wave antennas. This paper presents a methodology utilizing a parallel-plate waveguide with a metasurface as its top plate. Previous limitations on constant leakage factor are addressed using a slowly varying amplitude approximation in order to satisfy Maxwell's wave equation, enabling the design of the radiation pattern. A semi-analytical algorithm is employed to obtain the required multi-layer unit-cell geometries. Here, the inter-layer coupling is taken into account, enabling an efficient synthesis of these antennas. Several designs presenting different pointing angles and aperture field distributions are carried out, showing very good agreement between theory and realistic simulations without further full-wave optimization. Finally, the design process is experimentally validated through several prototypes, whose measurements are shown and discussed. These results, demonstrating straightforward semi-analytical synthesis of versatile aperture profiles, would significantly broaden the applicability of such antennas in next-generation wireless systems.**

***Index Terms*—Leaky-wave antennas, aperture control, Huygens' metasurface, unit cell synthesis.**

I. Introduction

EMERGING wireless communication systems increasingly require antennas with demanding specifications. For example, 5G/6G cellular networks, radars in autonomous vehicles, or satellite communications devices all have requirements for high directivity, beamforming, and scanning capabilities. In addition, these systems often have space constraints, where low-profile solutions are advantageous. Traditional phased array antennas are the most established solution for meeting these requirements. However, the feeding network needed by their several active elements can become quite complex, as well as considerably costly, in order to precisely control each signal phase independently [1]. As an alternative, leaky-wave antennas (LWAs) offer reduced complexity and simple feeding. LWAs have been studied since the last century [2], [3] and they still maintain the interest up to the day [4], [5]. These are travelling-wave structures for which the electromagnetic field is progressively radiated along its length. They are characterized by a wavenumber, composed of a phase constant and a leakage factor, which respectively control the output angle and the radiation rate. However, LWAs have traditionally suffered from a dependency between both parameters, which limits the flexibility in the achievable radiation characteristics.

The unique ability of metasurfaces (MSs) to manipulate electromagnetic waves at will has opened up a range of new possibilities, making them increasingly popular in recent years [6]. These metasurfaces are composed of several subwavelength particles able to synthesize a precise boundary condition in order to achieve a particular field transformation under certain wave illumination conditions. The design process usually comprises two phases: first, the *macroscopic* design consists of stipulating the fields and obtaining the corresponding metasurface parameters that synthesize the required boundary condition; then, the *microscopic* design is responsible for the physical implementation of the metasurface cells [7]. Some applications where MSs have been proposed include anomalous refraction [8]–[10], impedance matching [11], lenses [12], [13] or electromagnetic cloaking [14], [15]. In addition, metasurface-based antennas are also a rapidly emerging field of research due to their potential for enhanced versatility and efficiency [16]–[22]. In fact, due to the MSs' low-profile and precise control over the radiation characteristics, these antennas usually make use of leaky waves as the radiation mechanism. This way, by properly modulating the surface impedance, they transform propagating modes into leaky modes with specific amplitude, phase and polarization [23]–[25].

Huygens' metasurfaces (HMS) have been proposed in recent years as a powerful tool to achieve arbitrary wavefront manipulation [8], [26], [27]. These are composed of electrically- and magnetically-polarizable cells (Huygens' sources) that can induce precise electric and (equivalent) magnetic surface currents upon a given incident field. This way, the refracted field is completely defined, as stated by the equivalence principle, and so the desired field transformation is obtained [28]. In the design process, these HMSs are usually characterized by the use of *generalized sheet transition conditions* (GSTC) that relate the stipulated fields at both sides of the surface with the HMS parameters for that specific boundary condition [29]–[31]. In addition, according to [31], passive

This work was supported by the Spanish Ministry of Universities under Grant FPU20/03240 and by MICIU/AEI/10.13039/501100011033 and ERDF/EU under Grant PID2022-141193OB-I00. *(Corresponding author: Pablo Mateos-Ruiz)*

P. Mateos-Ruiz and E. Abdo-Sánchez are with the Telecommunication Research Institute (TELMA), University of Málaga, 29010 Málaga, Spain (e-mail: pablomr@ic.uma.es; elenaabdo@ic.uma.es).

V. K. Killamsetty and A. Epstein are with the Andrew and Erna Viterbi Faculty of Electrical and Computer Engineering, Technion–Israel Institute of Technology, Haifa 32000, Israel (e-mail: vinay.killamsetty@gmail.com; epsteina@ee.technion.ac.il).

Manuscript received XXXXX XX, 202X; revised XXXXX XX, 202X.

and lossless metasurfaces can be obtained by fulfilling a single local conservation condition when bianisotropy of the omega type is introduced in the HMS particles. These omega-type bianisotropic Huygens' metasurfaces (BHMS) have this ability thanks to the additional degree of freedom given by the magnetoelectric coupling between the surface currents. The advantageous characteristics of BHMSs offer great versatility for the macroscopic design in applications where the electromagnetic problem can be rigorously defined. For example, they have been used to convert a propagating wave into a surface wave with near-perfect efficiency [32], to successfully achieve electromagnetic invisibility in practical realizations [15], or to reduce the beam-squinting effect in LWAs [33].

In previous works, some of the authors developed a BHMS-based periodic LWA with several degrees of freedom by transforming a waveguide mode into a leaky mode [34]. The open stop-band effect was completely suppressed by allowing a single spatial harmonic to carry power without limitations in the selection of the period. In addition, independent control of the phase constant and the leakage factor was achieved, thus overcoming a main limitation of traditional LWAs. However, unlike other tapered LWA design methodologies where the leakage factor can be varied [5], [24], [35], the rigorous mathematical derivation of the BHMS-based LWA in [34] limited the wavenumber to being constant. This fact meant that the radiation pattern could not be engineered once the α and β values were chosen.

In this contribution, we fill this gap, extending the work in [34] to allow versatile radiation patterns using a simple, semi-analytically designed, LWA configuration. Starting from the same parallel-plate waveguide structure, the analytical derivation for the MS macroscopic design is modified in order to allow the inclusion of variable wavenumbers, thus enabling the design of arbitrary aperture field distributions on the metasurface, which leads to radiation pattern shaping capabilities. This approach was presented by the authors in [36], but not experimentally demonstrated. Some approximations are carried out in the wave equation resolution in order to simplify the design process. This way, the metasurface parameters (which are, in general, not periodic) are obtained for a given pointing angle and variable leakage factor related to the radiation pattern shape, once the rest of geometrical characteristics are fixed. In addition, a semi-analytical synthesis algorithm is exploited to physically realize the MS unit cells, composed of several stacked metalized substrates, taking into account the intra-cell mutual coupling between the several printed geometries. Finally, several LWA designs are carried out with different pointing directions, aperture distributions and radiation efficiencies, as to demonstrate the versatility of the methodology. Some of these designs are fabricated in order to verify the methodology through the obtained experimental results. The rigorous approach allows the synthesis of arbitrary aperture profiles, which is of tremendous impact and potential in the applicability of leaky-wave antennas, since the limitations of the exponential illumination is overcome. The achieved control of the radiation pattern, along with the semi-analytical method to obtain readily manufacturable metasurfaces, offers great versatility for highly-demanding antenna systems.

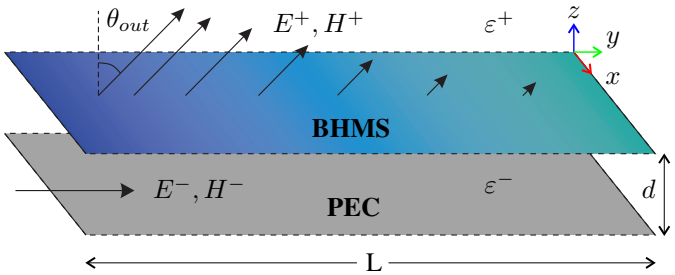

Fig. 1. Proposed LWA configuration.

II. Theory

A 2-D configuration is assumed, in which the BHMS is infinite and invariant in the x-coordinate. Placing a parallel PEC plate at a distance d below the BHMS would result in a variation of a parallel-plate waveguide, thus creating a guiding structure as shown in Fig. 1. The main objective of the BHMS will then be transforming the field propagating along its bottom side to a leaky-wave field with the desired characteristics at its top side. Furthermore, the BHMS can also enforce the necessary conditions for the guided field to propagate between both plates. Particularly, in this case the structure has a length L in the y-coordinate and is excited with a transverse electric (TE) polarized field ($E_y = E_z = H_x = 0$) at $y = 0$. The media above and below the metasurface are assumed non-magnetic and characterized by their relative electric permittivities ε_r^+ and ε_r^-, respectively. Both media present an intrinsic impedance $\eta^{\pm} = \sqrt{\mu_0/(\varepsilon_0 \varepsilon_r^{\pm})}$ and wavenumber $k^{\pm} = \omega\sqrt{\mu_0 \varepsilon_0 \varepsilon_r^{\pm}}$.

As with any metasurface theoretical synthesis, the first step is to stipulate the desired electromagnetic fields on both of its sides. In accordance with the proposed structure, a guided-wave mode is stipulated below the BHMS, inside the parallel-plate waveguide, while the desired field above the BHMS is stipulated as a leaky-wave mode radiating to the free space region at a certain angle with respect to the surface normal. The metasurface will impose the necessary boundary conditions at $z = 0$, so the only constraint for the guided field is to vanish at the PEC plane ($z = -d$), as described in [34]. However, in that previous work, the theoretical derivation constrained the wavenumbers to being constant. In this case, the goal is to engineer arbitrary aperture field distributions, for which spatially-varying wavenumbers are necessary. In order to take this variation into account, the field expressions from the previous work are modified, integrating the longitudinal wavenumber along the propagation direction (y-coordinate). Thus, the electromagnetic field below the metasurface is stipulated as

$$\begin{aligned} E_x^- &= |E_{\text{in}}| \left(e^{jk_z^-(z+d)} - e^{-jk_z^-(z+d)} \right) e^{-j\int_0^y k_y^-(\tau)\,d\tau} \\ &= 2j|E_{\text{in}}| \sin(k_z^-(z+d))\, e^{-j\int_0^y k_y^-(\tau)\,d\tau} \end{aligned} \tag{1a}$$

$$\begin{aligned} H_y^- &= \frac{j}{k^-\eta^-}\frac{\partial E_x^-}{\partial z} \\ &= -2|E_{\text{in}}|\frac{k_z^-}{k^-\eta^-}\cos(k_z^-(z+d))\, e^{-j\int_0^y k_y^-(\tau)\,d\tau} \end{aligned} \tag{1b}$$

while the expression of the required leaky mode in the region above the metasurface is

$$E_x^+ = |E_{\text{out}}|\, e^{-jk_z^+ z} e^{-j\int_0^y k_y^+(\tau)\,d\tau} e^{j\xi} \tag{2a}$$

$$\begin{aligned} H_y^+ &= \frac{j}{k^+\eta^+}\frac{\partial E_x^+}{\partial z} \\ &= |E_{\text{out}}|\frac{k_z^+}{k^+\eta^+}\, e^{-jk_z^+ z} e^{-j\int_0^y k_y^+(\tau)\,d\tau} e^{j\xi} \end{aligned} \tag{2b}$$

where ξ is an added degree of freedom indicating an optional constant phase shift of the wave.

The longitudinal and transverse wavenumbers are complex with attenuation factors α which are non-zero (to let the structure radiate):

$$\begin{aligned} k_y^-(y) &= \beta^- - j\alpha^-(y); \quad k_z^-(y) = \beta_z^-(y) - j\alpha_z^-(y), \\ k_y^+(y) &= \beta^+ - j\alpha^+(y); \quad k_z^+(y) = \beta_z^+(y) - j\alpha_z^+(y). \end{aligned} \tag{3}$$

As aperture field distribution control is desired, the transverse attenuation factors are dependent on the y-coordinate, while β is kept constant. Hence, as both wavenumbers will be related, the longitudinal wavenumber components will also be y-dependent, in general, as explicitly noted in (3).

The stipulated field expressions (1) and (2) must satisfy Maxwell's wave equation, whose solution will give the relation between the vertical and horizontal wavenumbers. For this particular case, as $\partial/\partial x = 0$ is assumed, the corresponding Helmholtz equation reduces to

$$\nabla^2\vec{E} + k^2\vec{E} = \frac{\partial^2 E_x}{\partial y^2} + \frac{\partial^2 E_x}{\partial z^2} + k^2 E_x = 0. \tag{4}$$

The partial derivatives of the electric field with respect to the z-coordinate are straightforward. They have the same form for (1) and (2) and their solutions are identical to those for the constant wavenumbers case:

$$\frac{\partial E_x^\pm}{\partial z} = -jk_z^\pm(y)E_x^\pm. \tag{5}$$

However, this is not the case for the partial derivatives with respect to y, as k_z is now dependent on this coordinate. By using the fundamental theorem of calculus, the following expressions are obtained:

$$\begin{aligned} \frac{\partial E_x^-}{\partial y} &= \left[(z+d)\frac{\partial k_z^-(y)}{\partial y}\cot\big((z+d)k_z^-(y)\big) - jk_y^-(y)\right]E_x^- \\ \frac{\partial E_x^+}{\partial y} &= -j\left[z\frac{\partial k_z^+(y)}{\partial y} + k_y^+(y)\right]E_x^+ \end{aligned} \tag{6}$$

Obtaining the second order derivatives from (5) and (6) and substituting them into (4), the complete relationship between wavenumbers for both regions of space, taking into account the variation along y, can be found to be a pair of quite intricate differential equations:

$$\begin{aligned} {k^-}^2 &= {k_y^-}^2(y) + {k_z^-}^2(y) \\ &\quad - (z+d)\cot\big((z+d)k_z^-(y)\big)\frac{\partial^2 k_z^-(y)}{\partial y^2} \\ &\quad + 2j(z+d)\cot\big((z+d)k_z^-(y)\big)\frac{\partial k_z^-(y)}{\partial y}k_y^-(y) \\ &\quad + (z+d)^2\left(\frac{\partial k_z^-(y)}{\partial y}\right)^2 + j\frac{\partial k_y^-(y)}{\partial y}, \\ {k^+}^2 &= {k_y^+}^2(y) + {k_z^+}^2(y) \\ &\quad + jz\frac{\partial^2 k_z^+(y)}{\partial y^2} + 2z\frac{\partial k_z^+(y)}{\partial y}k_y^+(y) \\ &\quad + z^2\left(\frac{\partial k_z^+(y)}{\partial y}\right)^2 + j\frac{\partial k_y^+(y)}{\partial y} \end{aligned} \tag{7}$$

These dispersion relations make it difficult to effectively design a metasurface with the described stipulated fields. Therefore, as explained in detail in Appendix A, a Slowly Varying Amplitude Approximation (SVAA) approach is assumed for the value of $\alpha(y)$. This allows neglecting its derivative, and the dispersion relation can be approximated by the common, simpler one:

$$\begin{aligned} {k^-}^2 &\simeq {k_y^-}^2(y) + {k_z^-}^2(y), \\ {k^+}^2 &\simeq {k_y^+}^2(y) + {k_z^+}^2(y). \end{aligned} \tag{8}$$

On the other hand, only the *local power conservation* condition needs to be fulfilled by the desired arbitrary field transformation in order to be realized with passive and lossless particles ($\text{Re}\{Z_{se}\} = \text{Re}\{Y_{sm}\} = \text{Im}\{K_{em}\} = 0$), according to [31]. This restriction implies that the real power must remain the same at both sides for each point along the metasurface, i.e. $P_z^-(y) = P_z^+(y)$ with $P_z = (1/2)\,\text{Re}\{E_x H_y^*\}$. In particular, the stipulated fields (1) and (2) yield the following power profiles, respectively:

$$\begin{aligned} P_z^-(y) = -\frac{|E_{\text{in}}|^2}{\eta^- k^-}\big(&\beta_z^-(y)\sinh(2\alpha_z^-(y)d) \\ &- \alpha_z^-(y)\sin(2\beta_z^-(y)d)\big)\, e^{-2\int_0^y \alpha^-(\tau)\,d\tau} \end{aligned} \tag{9}$$

$$P_z^+(y) = \frac{1}{2}|E_{\text{out}}|^2\frac{\beta_z^+(y)}{\eta^+ k^+}\, e^{-2\int_0^y \alpha^+(\tau)\,d\tau} \tag{10}$$

In order to satisfy the local power conservation constraint, one option is to impose that the fields have the same decay rate, even if they are spatially varying. This is, in fact, a generalization of the result presented in [34] in this context. Thus, $\alpha^-(y) = \alpha^+(y) = \alpha(y)$, where the latter is the leakage factor of the antenna. This way, the amplitude of the leaky field above the metasurface is fully determined from the rest of known values (y-dependencies omitted for compactness):

$$\frac{|E_{\text{out}}|}{|E_{\text{in}}|} = \sqrt{2\frac{\eta^+ k^+}{\eta^- k^- \beta_z^+}\left(\alpha_z^-\sin(2\beta_z^- d) - \beta_z^-\sinh(2\alpha_z^- d)\right)} \tag{11}$$

The value of $|E_{\text{out}}|$ will then be, in general, variable along y, in order to compensate for the power decay from $\alpha(y)$

and, thus, giving $P_z^+(y)$ the shape of the desired aperture distribution at the metasurface plane, and equal to $P_z^-(y)$.

Finally, the electromagnetic properties that the omega-type BHMS must present to achieve the required field transformation are obtained from the stipulated fields tangential components (1)-(2) immediately below and above the metasurface through the bianisotropic sheet transition conditions [31], [37], namely

$$\begin{aligned} \tfrac{1}{2}\left(E_x^+ + E_x^-\right) &= -Z_{se}\left(H_y^+ - H_y^-\right) - K_{em}\left(E_x^+ - E_x^-\right) \\ \tfrac{1}{2}\left(H_y^+ + H_y^-\right) &= -Y_{sm}\left(E_x^+ - E_x^-\right) + K_{em}\left(H_y^+ - H_y^-\right) \end{aligned} \tag{12}$$

where Z_{se}, Y_{sm} and K_{em} stand for the electric surface impedance, the magnetic surface admittance, and the magnetoelectric coupling coefficient, respectively, and they are also variable along the y-coordinate. Rearranging these expressions, the metasurface constituents can be obtained as a function of the tangential field components $[E_x^-, H_y^-, E_x^+, H_y^+]$ evaluated at $z \to \pm 0$ as follows [31]:

$$\begin{aligned} Z_{se} &= -j\left(\frac{1}{2}\,\mathrm{Im}\left[\frac{E_x^+ + E_x^-}{H_y^+ - H_y^-}\right] + K_{em}\,\mathrm{Im}\left[\frac{E_x^+ - E_x^-}{H_y^+ - H_y^-}\right]\right) \\ Y_{sm} &= -j\left(\frac{1}{2}\,\mathrm{Im}\left[\frac{H_y^+ + H_y^-}{E_x^+ - E_x^-}\right] - K_{em}\,\mathrm{Im}\left[\frac{H_y^+ - H_y^-}{E_x^+ - E_x^-}\right]\right) \\ K_{em} &= \frac{1}{2}\frac{\mathrm{Re}\left[E_x^+ {H_y^-}^* - E_x^- {H_y^+}^*\right]}{\mathrm{Re}\left[\left(E_x^+ - E_x^-\right)\left(H_y^+ - H_y^-\right)^*\right]}. \end{aligned} \tag{13}$$

Furthermore, in [34] it was demonstrated that, when α is constant, the values of $[K_{se}, Y_{sm}, K_{em}]$ are periodic with a period given as

$$p = \frac{2\pi}{|\beta^+ - \beta^-|}. \tag{14}$$

This periodicity expression is in accordance with Floquet's theorem, usually applied to periodic leaky-wave antennas analysis. In fact, (14) indicates that the LWA radiates from one of the first higher order spatial harmonics ($m = \pm 1$), and the metasurface guarantees that no power is transferred to any other mode. However, once the wavenumber is variable, the metasurface constituents will cease to be periodic, in general. Nevertheless, the metasurface theoretical derivation guarantees the correct operation of the field transformation due to the uniqueness theorem. In fact, the exact conversion from the guided mode to a single leaky mode also guarantees the suppression of the open-stopband effect.

III. Design Methodology

The selection of the key LWA properties, namely the pointing angle and the desired radiation pattern, is the first step to carry out a design. The pointing angle θ_{out}, as well as the angle of incidence θ_{in} inside the parallel-plate waveguide, can be related to the phase constants above and under the metasurface β^+ and β^-, respectively, by [3]:

$$\begin{aligned} \beta^+ &\simeq k^+ \sin(\theta_{out}) \\ \beta^- &\simeq k^- \sin(\theta_{in}). \end{aligned} \tag{15}$$

On the other hand, a proper control of the radiation pattern requires a leakage factor $\alpha(y)$ decoupled from the phase constant values. Indeed, from the theoretical derivation it is clear that an independent control of the leakage factor is possible, without any restrictions related to other antenna properties. After deciding the antenna length L, and knowing the desired aperture field distribution expression $|A(y)|$, a well-known LWA approximate expression can be used to extract the required leakage factor along the y-coordinate [3]:

$$\alpha(y) = \frac{1}{2}\frac{|A(y)|^2}{\frac{1}{\eta_{rad}}\int_0^L |A(\tau)|^2\,d\tau - \int_0^y |A(\tau)|^2\,d\tau}, \tag{16}$$

where η_{rad} is the radiation efficiency, which can be calculated as $1 - P_z^-(L)/P_z^-(0)$. In order to better exploit the aperture area, the power remaining at the end of the aperture $P_z^-(L)$ should be as low as possible. However, as its value approaches zero, then $\alpha(y)$ becomes very large when $y \to L$. Although this behavior is general for tapered LWAs, it is mostly relevant for the BHMS-based LWA discussed herein, as the validity of (8) depends on the taken SVAA approach, which assumes that the leakage factor value changes slowly. Thus, the use of very high values of η_{rad} could invalidate the theoretical derivation in Section II.

It also must be taken into account that (16) is an approximation that assumes that the power decay in the aperture only depends on the $\alpha(y)$ value, i.e. that the vertical field profile remains unchanged for every transversal cut of the waveguide, which implies that k_z^- is constant in (1). Although this condition is roughly satisfied by the SVAA, if $\alpha(y)$ varies sufficiently along the antenna length, it will affect the value of $k_z^-(y)$, which will consequently influence the real power at the metasurface plane, as deduced from (9). This issue could be solved by numerically optimizing the value of the leakage factor to obtain a precise power profile but, for the sake of simplicity, the value from (16) is kept, as it should be accurate enough.

Once the phase constants and leakage factor are specified, every wavenumber, both horizontal and vertical and for both regions of space, is uniquely defined by (8). Thus, the waveguide height d is another degree of freedom, such as the incidence angle θ_{in}, having the radiation and waveguiding problems effectively decoupled. In fact, the BHMS will force the boundary conditions necessary for the electromagnetic field to propagate below it, without forcing any relation between d and θ_{in}, and even when the waveguide height would be small enough, in normal circumstances, to put the waveguide under cutoff.

With all the parameters set, the macroscopic design is completed. For the microscopic counterpart, the metasurface must first be discretized along the y-coordinate in order to allow the physical implementation of the theoretically continuously-varying boundary condition. Thus, the BHMS is subdivided into its meta-atoms, which will be sub-wavelength in size to allow a fine sampling of the required metasurface constituents $\{Z_{se}, Y_{sm}, K_{em}\}$. In this case, the sampling rate and, consequently, the meta-atoms' length, is chosen to be $\Delta_y = \lambda_0/4$, which could be considered as *aggressive discretization* since it is not considerably smaller than a wavelength. Nevertheless, bigger unit cells pose an advantage, easing the manufacturing

process, as long as the homogenization approximation keeps working, which has been verified by numerical simulations.

Each meta-atom implements the local properties of the metasurface at a given $y = n\Delta_y$, with $n = 1, 2, \ldots, \lfloor L/\Delta_y \rfloor$, by assuming local periodicity, i.e. that the scattering properties of the meta-atom can be approximated by those evaluated when the meta-atom is embedded in a uniform infinite periodic array. In this way, from a microwave network perspective, an equivalent circuit can be obtained for each unit cell, characterizing it as a 2×2 impedance matrix [**Z**] which relates the local tangential fields below and above the metasurface [38].

$$\begin{pmatrix} E_x^- \\ E_x^+ \end{pmatrix} = \begin{pmatrix} Z_{11} & Z_{12} \\ Z_{21} & Z_{22} \end{pmatrix} \begin{pmatrix} H_y^- \\ -H_y^+ \end{pmatrix} \tag{17}$$

Substituting (17) into (13) and rearranging, the different impedance matrix elements can be expressed in terms of the metasurface parameters [31], as follows:

$$\begin{aligned} Z_{11} &= Z_{se} + \frac{(1+2K_{em})^2}{4Y_{sm}}, \\ Z_{12} = Z_{21} &= Z_{se} - \frac{(1-2K_{em})(1+2K_{em})}{4Y_{sm}}, \\ Z_{22} &= Z_{se} + \frac{(1-2K_{em})^2}{4Y_{sm}}. \end{aligned} \tag{18}$$

These Z-matrices can be converted to S-matrices, which may be more insightful on the unit cell behavior. In this sense, the LWA will partially transmit and reflect the leaky guided mode at each point. Thus, the reflection and transmission scattering parameters may adopt any given passive magnitude, in order to fulfill the required leakage factor function from (16). Furthermore, these parameters will need to present any given phase value, determined by the specific design requirements. Therefore, the unit cell should be able to synthesize any arbitrary lossless, reciprocal 2×2 S-matrix.

IV. Physical Implementation

A common ideal way of implementing these impedance parameters is with stacks of three impedance sheets cascaded by dielectric substrates, as shown in Fig. 2a. Under plane-wave illumination, and provided that near-field coupling effects can be neglected, this structure can be modelled with parallel admittances representing the impedance sheets and transmission lines for the dielectrics between them, as depicted in Fig. 2b. As the magnetoelectric coupling coefficient K_{em} is non-zero due to the bianisotropy of the BHMS, the three different components of the reciprocal lossless Z-matrix can be directly related to the three degrees of freedom given by the purely-imaginary parallel reactances through closed-form expressions [31], once the dielectric properties are fixed. Thus, the circuit model allows simple synthesis of the required unit-cell parameters, as each layer can be independently designed to present the needed impedance.

The implementation of the meta-atoms with real geometries entails several challenges, due to the difficulty of synthesizing the lossless scattering properties required by any BHMS design. Starting from the ideal three stacked impedance sheets configuration, the first question arises on how to achieve

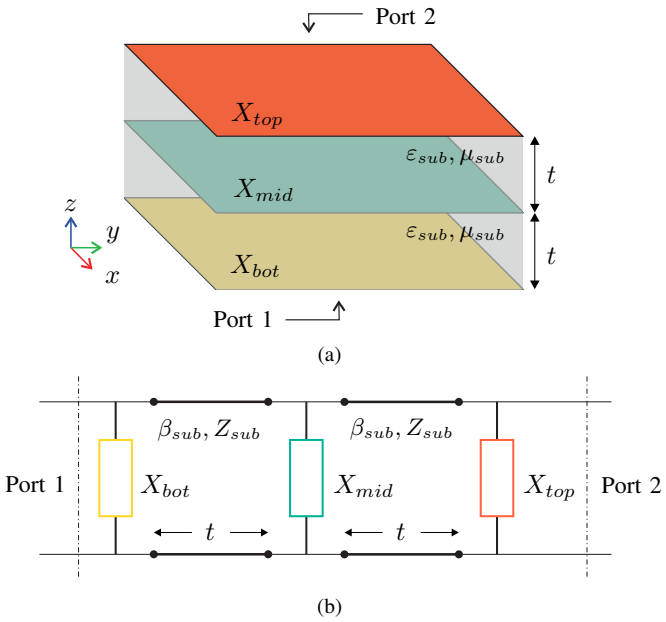

Fig. 2. Ideal three stacked impedance sheets meta-atom configuration. (a) Illustration and (b) corresponding equivalent circuit based on a transmission line model.

the required reactance values for each layer. Usually, different geometries are printed on the copper metallization layers of the dielectric substrates. Depending on the shape of these copper traces, a wide range of impedance values can be synthesized under plane-wave illumination. However, the metal used for these geometries, as well as the dielectric substrates over which they are printed, will present non-zero resistances, which will materialize as losses. Therefore, the actual impedance sheets will not be purely reactive and the practical implementation will diverge from the theoretical design. Furthermore, as already stated in [34], for this LWA application in particular, smaller values of θ_{in} mean that the wave impinges more times on the metasurface, which translates into an increase in total losses.

On the other hand, although the ideal stack of three pure-reactance sheets is a suitable configuration for proofs-of-concept in simulations, it offers an unique solution for the required reactance values. Thus, depending on the specific properties needed for a meta-atom, those required values could be considerably hard to correctly synthesize. For example, a required reactance could be very small, which is hard to achieve in practical implementations with a sufficiently low resistance in comparison. Or, assuming that the chosen printed geometry is capable of synthesizing any reactance value (which is not usually the case either), its associated resistance is fixed, with very little to no loss minimization capability. Therefore, configurations with more than three impedance layers are often used, thus increasing the available degrees of freedom and broadening the solution space [34], [39]. This way, there is a higher probability of finding a set of printed geometries that better adjust the scattering parameters of a given unit cell, and resulting in lower total losses.

Increasing the number of layers, however, entails more complexity in the design. There is no initial solution for

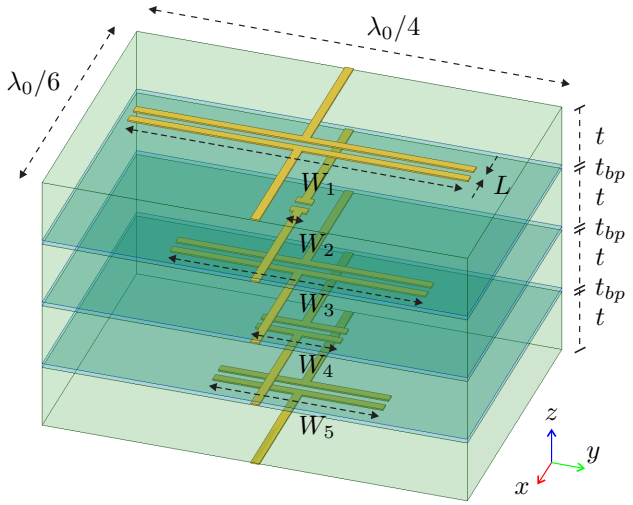

Fig. 3. Real unit cell configuration with 5 copper layers.

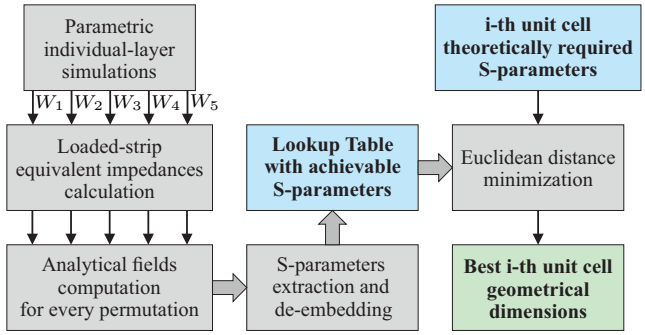

Fig. 4. Block diagram of the semi-analytical unit-cell synthesis algorithm.

the reactance values (the closed-form expressions in [31] do not hold anymore), thus their optimization becomes more complicated. In addition, as more layers are used, the total BHMS thickness grows, which usually deteriorates its performance due to lateral field interactions between adjacent unit cells [40]. In this sense, thinner substrates are preferred. Furthermore, when real implementation is considered, the near-filed coupling between the copper traces of the different layers can invalidate the simple transmission line model.

In this work, the dimensions of the unit cells are $\lambda_0/6 \times \lambda_0/4$. Four Rogers RO3003 ($\varepsilon_r = 3$) laminates of thickness $t = 30\,\text{mil}$ each are stacked and bonded with 2 mil thick Rogers 2929 Bondply ($\varepsilon_r = 2.94$) laminates, resulting in a total unit-cell height of $\lambda_0/6.25$. The copper traces are $18\,\mu\text{m}$ thick, have a width of $0.1\,\text{mm}$ and consist of dogbone, or dumbbell, shapes in every layer, as shown in Fig. 3. In addition, the media above and below the BHMS are assumed to be vacuum ($\varepsilon^- = \varepsilon^+ = \varepsilon_0$).

The low permittivity of the laminates, in addition with their thin thickness, are the right combination to favor a strong near-field coupling between layers. In fact, it has been experimentally verified through electromagnetic simulations that the simple equivalent circuit does not properly model the chosen meta-atom configuration. Thus, electromagnetic coupling between the different copper traces must be taken into account.

Following the approach presented in [41]–[43], and recently implemented in [44], the scattering parameters of the meta-atoms can be obtained through a systematic formulation that addresses the near-field phenomena. This scheme analytically calculates the fields scattered by the stratified media configuration and the ones produced by the induced currents in the copper traces. For this specific implementation of the synthesis methodology, the conductor geometries are capacitively-loaded strips with a variable capacitor width W_n, n being the layer number. This specific copper geometry is needed to be able to model it as a wire with an associated effective load impedance, which will directly relate to the induced currents from which the near-field interactions can be computed. This was the reason for the use of this specific geometry in the first place and, thus, a very small $L = 0.1\,\text{mm}$ is chosen as the capacitor strips separation for all layers.

The semi-analytical unit-cell synthesis algorithm is summarized in the diagram depicted in Fig. 4, and explained as follows. In order to obtain the equivalent impedance of the loaded strips, parametric electromagnetic simulations are carried out for every copper strip placed alone in its interface within the complete layered substrates configuration. These simulations are performed in Ansys HFSS, under normally-incident, TE-polarized plane wave excitation from Floquet ports, and with periodic master-slave boundary conditions. The capacitor width is swept in the range $W_n \in \{0.1, 0.2, ..., 4.9\}$ for every individual-layer simulation. The ports are referenced to the same plane, which is the first air-substrate interface from the bottom of the cell. This way, from the reflection and transmission coefficients of these simulations, using the expressions from [42], the equivalent impedances of the loaded strips for every W_n are calculated in the absence of the other ones. Then, using those values, the external, scattered and strips-induced fields are analytically computed for all the possible permutations of W_n for the five layers. Note that only single-layer HFSS simulations are needed, and not for multilayer, which results in combinatorial savings. This way, a Lookup Table (LUT) is created containing the achievable local S parameters [related to the Z-matrix in (17)], corresponding to all the realizable meta-atoms with capacitor widths $\{W_1, W_2, W_3, W_4, W_5\}$.

The scattering coefficients obtained from the previous scheme are referenced to the vacuum intrinsic impedance η_0 and both ports are placed in the same plane. Thus, to get the S parameters conveniently calculated at the planes interacting with the outer regions, all S-matrices in the LUT are de-embedded to have the second port referenced to the substrate-air interface at the top of the mate-atom. Finally, the best geometrical parameters for every unit cell in a design are chosen by searching for the S-matrix from the LUT that minimizes the difference with respect to the required ones. This difference is computed as the Euclidean distance as follows:

$$\Delta S = |\hat{S}_{11} - S_{11}|^2 + |\hat{S}_{21} - S_{21}|^2 + |\hat{S}_{22} - S_{22}|^2, \quad (19)$$

with the hat symbol indicating the goal unit-cell parameters. This method has given better results in general than com-

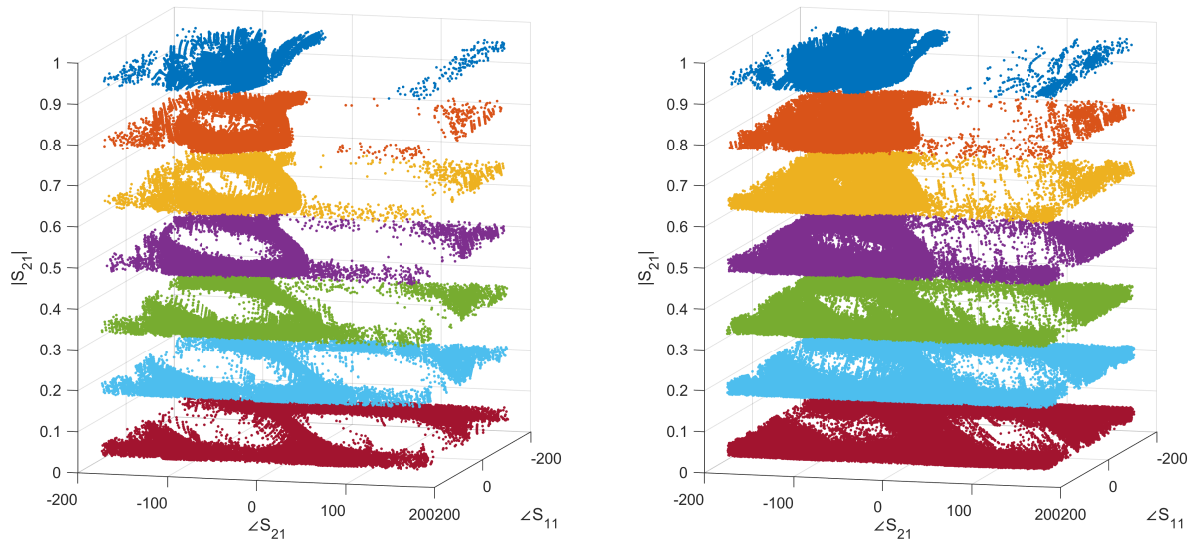

Fig. 5. Achievable S Parameters with losses limited to a maximum of 10% for the (a) 4 layers and (b) 5 layers unit-cell configurations. Several cuts of the complete LUT of synthesizable parameters are plotted to facilitate a qualitative visualization.

puting the difference as a sum of weighted errors for the coefficients magnitude and phase separately. In summary, this semi-analytical approach outputs the final dimensions of a unit-cell for any desired scattering parameters it is desired to offer. Furthermore, it is able to do so while taking into account the near-field coupling phenomena, so the unit cell substrate thickness can be chosen as thin as desired. Finally, only individual-layer simulations are carried out, with the associated time savings by avoiding any complete unit-cell simulation.

As the copper traces are restricted to present capacitive responses, potentially better solutions requiring inductive loads are not considered. For this particular meta-atom configuration, at least five impedance layers have been necessary to synthesize a suitable range of amplitude and phase values for both reflection and transmission of the S parameters. This is clearly shown in Fig. 5, where a fraction of the whole set of achievable S parameters is represented, as to give a qualitative view of how much of the potentially required solution space is fulfilled with the obtained LUT. Although the transmission coefficient magnitude $|S_{21}|$, its phase $\angle S_{21}$ and the reflection coefficient phase $\angle S_{11}$ do not completely describe the S-matrix when it is not lossless, it does give an approximate idea of the synthesizable values as losses are limited up to 10%. It can be observed that the same meta-atom configuration with only four copper layers lacks a considerable portion of the solution space (Fig. 5a), especially in comparison with its five-layers counterpart (Fig. 5b).

It is worth noting that the angle of incidence inside the LWA waveguide will not be normal to the BHMS. Therefore, formally, the characterization of the BHMS meta-atoms should be obtained under plane wave excitation with an incidence angle determined by the θ_{in} of the desired design. In this sense, a single dogbone-shaped copper geometry has been characterized in simulations under periodic boundary conditions and oblique incidence, with a semispace filled with air and the other with Rogers RO3003. Fig. 6 shows the obtained equivalent parallel impedance for a range of angles. The observed reactance variation is low, so the scattering properties will change with the incidence angle mainly due to the different impedance mismatches produced by the change in the wave impedance as $Z_{wave} = \eta/\cos\theta_{in}$. Consequently, as the complete unit cells are electrically thin, the scattering behavior of the metasurface can be approximated as that characterized for normal incidence, for angles that do not deviate much from it.

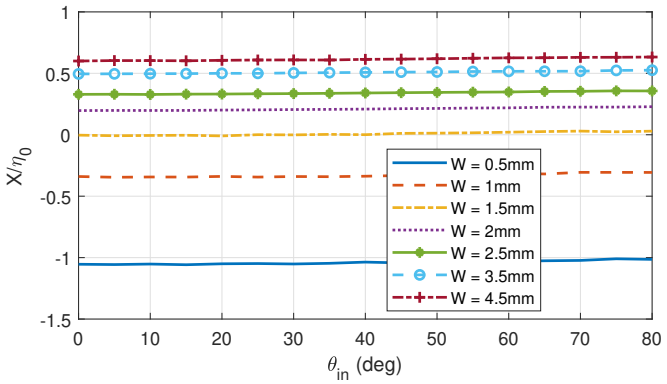

Fig. 6. Normalized equivalent parallel reactance of a single copper geometry with respect of the obliquely-incident plan wave angle, for different capacitor widths.

V. Designs and Simulation Results

A. Designs description

Several designs are carried out in order to test the validity of the theoretical derivations and the synthesis methodology. Three different pointing angles have been chosen along with several goal radiation patterns, to verify that the LWA properties can be selected at will while successfully enforcing

TABLE I
LWA PARAMETERS FOR THE DIFFERENT DESIGNS.

Parameter	Design 1	Design 2	Design 3
θ_{out} [°]	0	-30	60
θ_{in} [°]	26.4	30	21.5
$p\,[\lambda_0]$	9/4	4/4	8/4

the required aperture field distribution. For each pointing angle, a design is carried out without engineering the aperture distribution, i.e. with a constant α, for which the periodic nature of the LWA can be observed. This period relates θ_{in} with the value of θ_{out} through the expressions (14) and (15). This way, subsequent designs that implement variable leakage factors use the previously obtained θ_{in}, although there is no longer a physical period relating it to the pointing angle.

These designs are all carried out at 15 GHz, which is the same frequency for which the meta-atoms have been characterized. In addition, they all have a total length of $L = 10\lambda_0$ in order to obtain a fair comparison between them and facilitate the experimental validation with the same fabricated waveguide. For the latter reason, all the metasurfaces are also conceived for a waveguide of height $d = 0.5\lambda_0$ and filled with air. The rest of the parameters for each design is described in Table I. The three designs cover representative cases, namely broadside radiation for Design 1 (special and complicated case for LWAs due to the open stop-band issue), backwards radiation for Design 2 and extreme-angle beam for Design 3 (which radiates from the opposite spatial mode than the other designs). The chosen values of θ_{in} are not considerably high in order to enable the use of the normal-incidence characterization of the unit cells, as discussed in Section IV. In addition, those values, which are similar for all the designs, guarantee an electric field profile inside the waveguide that would be under cut-off if no BHMS was used, thus showcasing yet another of its capabilities. Nevertheless, the field profile is similar to that of a typical TE_{10} mode for HFSS to be able to successfully converge.

The aperture distribution is also modified for each pointing angle. In particular, applying Uniform and Hamming windows, respectively

$$|A(y)|\big|_{\text{Uniform}} = 1\,, \tag{20}$$
$$|A(y)|\big|_{\text{Hamming}} = 0.54 - 0.46\cos(2\pi y/L)\,, \tag{21}$$

with different required radiation efficiencies, in addition to the base constant-α variants. By using (16), the required dependency for the leakage factor of each design is calculated, and shown in Fig. 7. A variety of combinations for the aperture distribution and radiation efficiency are selected in order to obtain a wide range of examples. The chosen radiation efficiencies are also considerably high to test the applicability of the SVAA approach also in these extreme limiting cases. Also, it can be noted that the variation in $\alpha(y)$ does not depend on the pointing angle. Hence, for example, the curves for the Hamming aperture with $\eta_{rad} = 99\%$ are equal for Designs 2 and 3.

As specified in Table I, the periods are chosen to be natural number of times the length of the unit-cells ($\lambda_0/4$) so that,

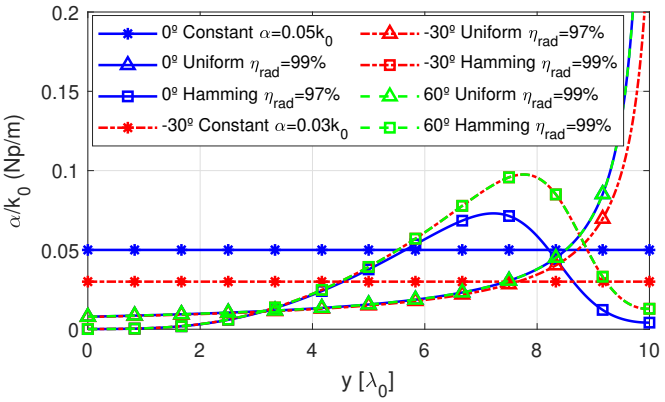

Fig. 7. Comparison of the leakage factor functions for each design. Blue, red and green lines are variations of the Designs 1, 2 and 3, respectively.

for the constant α cases, only the unit-cells inside one period must be synthesized, and then they are periodically reused. However, as the metasurfaces are no longer periodic when the aperture field distribution is engineered to manifest spatially-varying decay coefficients $\alpha(y)$, every unit cell along the antenna length will be, in general, different from the others. Consequently, the fact that the meta-atoms are synthesized following the unique semi-analytical approach described in Section IV, leading to fabrication-ready layouts without any further full-wave optimization, possess a great advantage for the efficient realization of these designs.

With the previous parameters, the wavenumbers are completely defined using (8) and the fields are calculated with (1) and (2). Hence, for each design, those field values are input into (13) to obtain the BHMS parameters (computed only at discrete steps related to the meta-atoms coordinates, as discussed in Section III), which can be converted to the impedance matrices required for each meta-atom through (18). Finally, these are transformed to the S-matrices for which the synthesis algorithm will find the closest ones in the LUT, as defined in (19).

As an illustrative example, the goal and semi-analytically synthesized (Section IV) S-parameters for each unit cell of the Design 2 with Hamming window aperture distribution are shown in Fig. 8. In addition, the scattering properties of those unit cells, individually obtained via full-wave simulation under periodic conditions, are also displayed. A very high similarity between the desired and achieved parameters is noted for all unit cells, thus demonstrating the great accuracy of the algorithm predictions.

B. Simulation Results

In order to carry out the full-wave simulation of the designs in Ansys HFSS, PEC sheets are placed on planes $x = \pm\lambda_0/12$ to emulate the x-axis infinite periodicity needed for the desired TE mode. This allows for the use of only one row of meta-atoms along the antenna length. In addition, a current line source in the x-axis is used as excitation instead of a waveport, as the excited field profile of the latter would not match that inside the waveguide. These simulations are computationally intensive, converging in around 7 hours on average and using

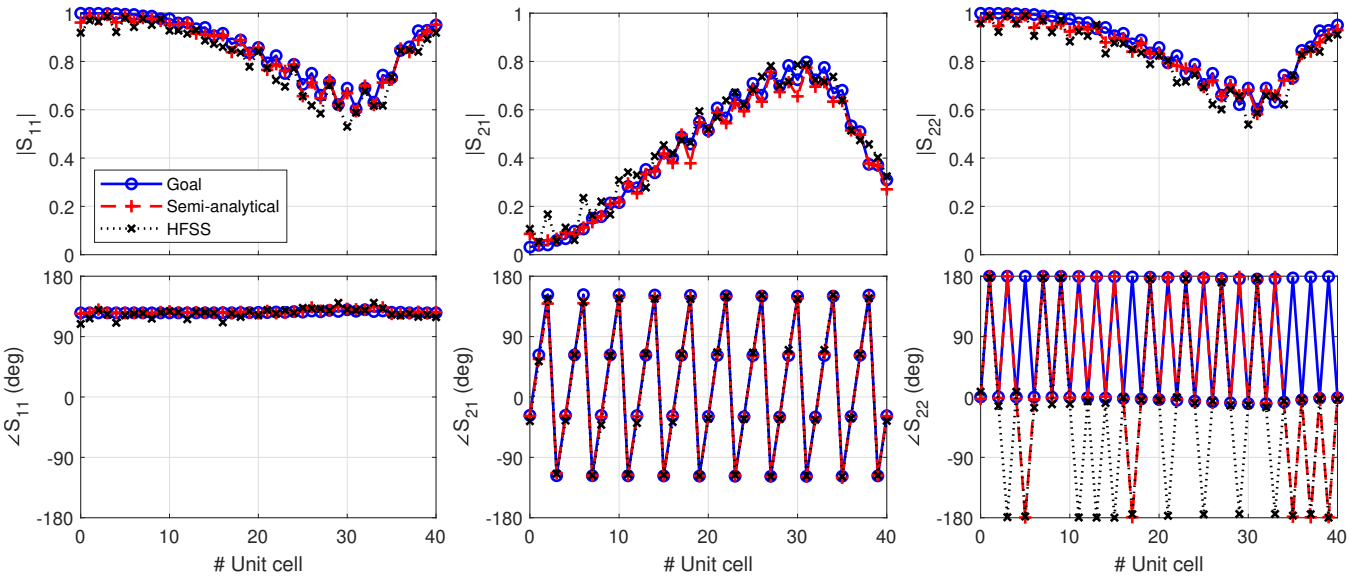

Fig. 8. Unit cell S-parameters for Design 2 with Hamming window aperture distribution.

TABLE II
FIGURES OF MERIT OF THE PRESENTED DESIGNS.

Design	θ_{out} (°)	D_{max} (dBi)	η_{ap} (%)	η_{rad} (%)	SLL (dB)
Design 1					
Constant (Theory)	0	15.9	61.4	99.8	-
Constant (Ideal Sim.)	0.1	15.4	55.5	99.6	-19.6
Constant (Real. Sim.)	0.4	14.8	48.5	99.9	-25.4
Uniform (Theory)	0	18.1	100	99	-13.5
Uniform (Ideal Sim.)	-0.4	17.8	94.8	97.7	-12.8
Uniform (Real. Sim.)	0.6	17.5	89.4	99.9	-10.9
Hamming (Theory)	0	16.6	73.5	97	-43.6
Hamming (Ideal Sim.)	-1.2	16.4	69.4	96.2	-13.5
Hamming (Real. Sim.)	-0.1	16.0	63.1	99.2	-14.6
Design 2					
Constant (Theory)	-30	16.4	70.2	97.7	-
Constant (Ideal Sim.)	-29.8	16.9	77.7	93.0	-18.8
Constant (Real. Sim.)	-27.4	16.0	62.7	99.1	-11.9
Uniform (Theory)	-30	17.4	88.2	97	-12.6
Uniform (Ideal Sim.)	-30	17.2	83.7	87.5	-13.2
Uniform (Real. Sim.)	-28.7	17.2	83.0	99.2	-11.7
Hamming (Theory)	-29.5	16.0	63.8	99	-41.4
Hamming (Ideal Sim.)	-28.8	15.5	56.2	95.8	-11.8
Hamming (Real. Sim.)	-29.1	15.4	54.7	99.9	-14.7
Design 3					
Uniform (Theory)	59	15.3	53.3	99	-10.7
Uniform (Ideal Sim.)	59.1	14.8	47.7	99.7	-10.5
Uniform (Real. Sim.)	58.3	14.4	43.9	99.9	-9.3
Hamming (Theory)	58	14.0	40.2	99	-37.8
Hamming (Ideal Sim.)	58.7	13.5	36.0	97.7	-11.2
Hamming (Real. Sim.)	57	13.0	31.4	99.9	-10.0

up to 100 GB of RAM in a 24 logic cores computer running a 2020th 4 GHz AMD processor. Therefore, ideal simulations are previously carried out as an intermediate step, using ideal unit cells like the one shown in Fig. 2a. These can be simulated using impedance boundary conditions, which allows reaching a good convergence in under 30 minutes using a maximum of 300 GB of RAM.

For brevity, only one aperture distribution case of each of the three designs is shown in Fig. 9, where a comparison of the electric field magnitude along the yz plane between the theoretical derivation [based on (1)-(2)] and the realistic simulation results (using the unit cells from Figs. 3 and 5b) is displayed. A very good agreement can be observed for the three shown cases. As designed, each case presents a different output angle while all having a similar input angle. It can also be noted how the field profile inside the waveguide is slightly cut before it reaches a null at $z = 0$ and, yet, the BHMS guarantees its propagation.

The leftmost (Figs. 9a, 9d) and rightmost (Figs. 9c, 9f) displayed cases, respectively Design 1 and Design 3, both present a uniform aperture, employing (20). This is clearly visible as the power radiated along the metasurface remains relatively constant, even though the power inside the waveguide clearly decays. Unlike a constant-α case, this allows taking advantage of all the antenna extent while radiating the majority of the available power before it reaches the end, thus achieving both high aperture and radiation efficiencies. The center displayed design (Figs. 9b, 9e) is the Hamming aperture case of Design 2, which employs (21). In this case, the field is mainly radiated at the middle of the BHMS, which will translate into lower secondary lobes at the expense of a lower aperture efficiency. The interaction of the field with the metasurfaces in the realistic simulations can be appreciated in the bottom figures at $z \approx 0$.

The associated 2D directivity diagrams are shown in Fig. 10, where a very good agreement between theory and simulations can be observed. It can be noted that some undesired secondary lobes appear, although some of them are already present in the ideal simulations. Thus, they may be caused by the very high values chosen for the radiation efficiency, which could take the SVAA approach beyond its strict validity, thus exciting spurious spatial modes. Regardless, the three shown cases present very high radiation efficiencies and, still, the used methodology holds. The step from the ideal reactance metasurfaces to the realistic ones does not considerably degrade the radiation characteristics, as can be noted from

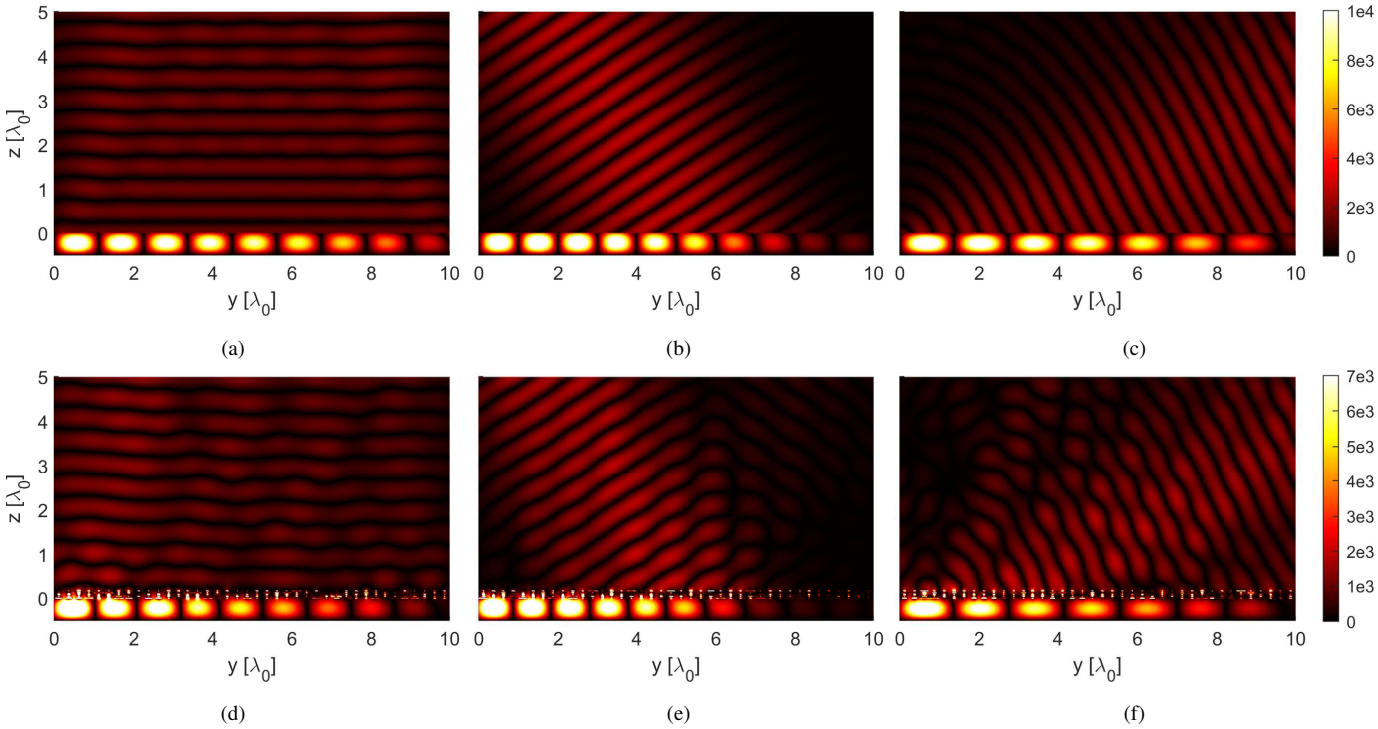

Fig. 9. Field distributions $|\mathrm{Re}(E_x(y,z))|$ (V/m): (a)-(c) theoretical prediction and (d)-(f) realistic electromagnetic simulation for (a, d) Design 1 and (c, f) Design 3 with Uniform apertures, and (b, e) Design 2 with Hamming aperture.

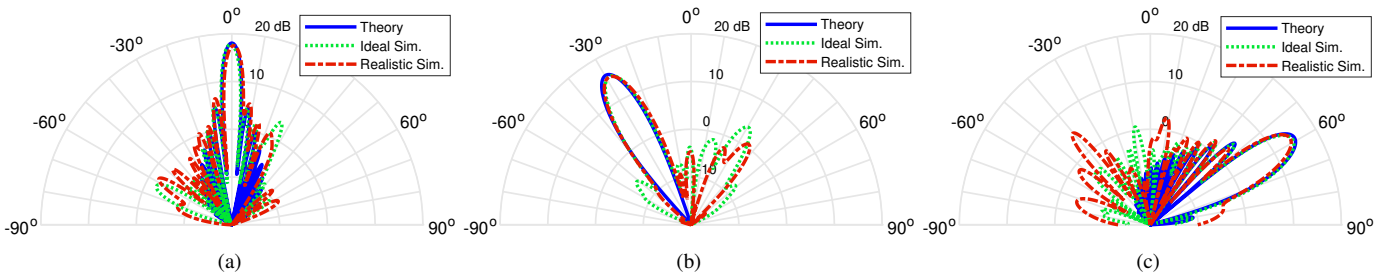

Fig. 10. 2-D directivity radiation patterns in the yz plane from theoretical derivation and electromagnetic simulations: (a) Design 1 with Uniform aperture, (b) Design 2 with Hamming aperture, and (c) Design 3 with Uniform aperture.

the figures of merit in Table II, where a high similarity between theory and simulations is observed for all the designs. This demonstrates the potential of the synthesis methodology, taking into account that no full-wave optimization of the unit cells nor the complete BHMS has been carried out.

VI. Experimental Validation

To demonstrate and verify the presented theoretical concept in practice, three BHMS prototypes have been fabricated, corresponding to Design 2 with the three different aperture field distributions. Pasternack PE44343 SMA connectors are used to feed these antennas. The connector is inserted at the beginning of the waveguide through a lateral wall with the pin exposed in the x direction to excite the TE mode of interest. In order to avoid any disturbances that the coupling from the feeding-probe coaxial mode to the waveguide mode may cause in the BHMS performance, non-radiating sections are added to both ends of the fabricated metasurfaces. These sections have a length of $\lambda_0/2$ (2 unit cells long) and ensure that the guided mode presents the profile that the radiating BHMS section expects, thus guaranteeing good matching between sections.

The unit cells of these edge sections must be non-radiating. Consequently, they are grounded at the top, making their implementation much simpler, as only the S_{11} parameter must be synthesized. By using the formulas from Section III with the parameters corresponding to Design 2 in Table I while imposing $\alpha = 0$, then a required $S_{11} = e^{j125.3^\circ}$ is obtained. The unit-cell geometry consider here only presents the copper dogbone of the bottom layer (see Fig. 3), and the remaining layers are totally metalized. The value of W_5 is swept in an HFSS parametric simulation of the complete described configuration, obtaining the synthesizable S_{11} values. Hence, in this case, $W_5 = 0.87\,\mathrm{mm}$ achieves the reflection coefficient which is maximum in magnitude and closest in phase to the required one.

The exact location where the connector is inserted to achieve a good matching is obtained by a parametric analysis in HFSS. It is carried out using the ideal impedance boundary conditions to speed up the process, and the chosen location is then verified

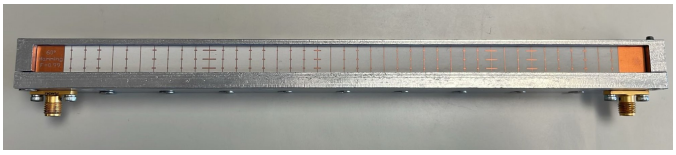

Fig. 11. LWA prototype with one of the designed metasurfaces mounted.

in a realistic simulation. Thus, the coaxial probe is inserted at $\Delta y = 4\,\mathrm{mm}$ from the start of the waveguide, $\Delta z = 5.6\,\mathrm{mm}$ from the bottom (where the field profile has its maximum), and the exposed pin penetrates $\Delta x = 2.33\,\mathrm{mm}$ into the guide. This point is selected as it provides a relatively good matching along all the designs, thus allowing the use of the same manufactured waveguide for all the measurements. In addition, another coaxial connector is inserted into the mirrored location at the end of the waveguide to have a completely closed structure. This ensures that the remaining power at the end of the waveguide can be dissipated in a matched load, and avoids possible problems derived from leaving the end of the waveguide open, like unwanted reflections. In fact, this complete feeding configuration is simulated to obtain the η_{rad} values from Table II. For the realistic simulations, load termination and ohmic losses are represented together by this efficiency, consequently higher values are expected. As seen, the theoretical and simulation values are in good agreement, with very high values in general, guaranteeing almost no power is dissipated at the load.

However, unlike in simulations, the metasurfaces are finally fabricated with three rows of meta-atoms along the x-axis, in order to physically force the desired periodicity to an extent, anticipating manufacturing tolerances. These metasurfaces were manufactured by Printech Circuit Laboratories Ltd. As the waveguide is now three times wider than initially simulated, the depth of the inserted coaxial probe must be readjusted. A new $\Delta x = 3.5\,\mathrm{mm}$ is obtained from parametric simulation with ideal impedance boundary conditions, as HFSS was not able to correctly complete realistic simulations with the three-rows BHMSs.

The waveguide itself was manufactured in two longitudinal aluminum pieces at the University of Málaga. Both pieces were CNC-machined and then assembled together using metallic screws, as shown in Fig. 11. The waveguide walls extend $2\,\mathrm{mm}$ above the BHMS top height in order to ensure that the conductor condition at both of its sides is sufficiently satisfied. Due to fabrication errors, the coaxial connectors holes were located at a displaced $\Delta y = 4.42\,\mathrm{mm}$ which, although not optimum, should provide an acceptable matching. Each fabricated metasurface is mounted into the waveguide and measured in an anechoic chamber at the University of Málaga. A matched load is connected to the end port, and the yz plane radiation is measured between 12 and 18 GHz.

An overview of the measurements results in comparison with those from realistic simulations is shown in Fig. 12, where the maximum 2D directivity and the main pointing angle as functions of frequency are shown for the three aperture distribution cases. The bottom graph only shows the pointing angle for the bands of interest, in order to avoid

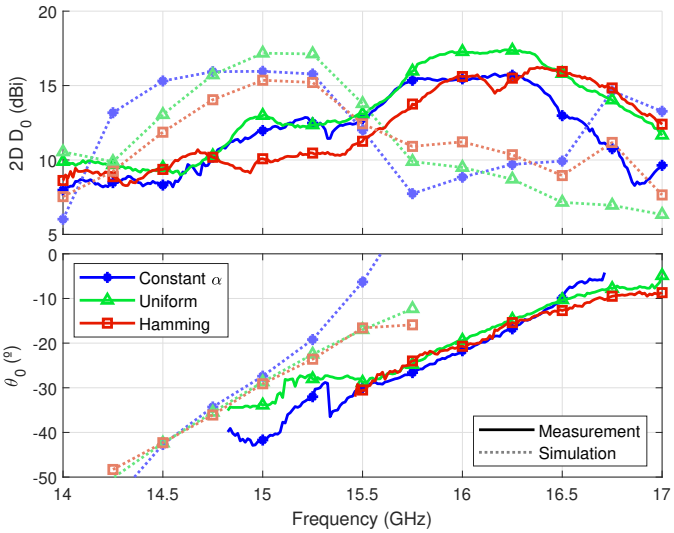

Fig. 12. Measured and simulated maximum 2D directivity (top) and corresponding pointing angle (bottom) for the three aperture cases of Design 2.

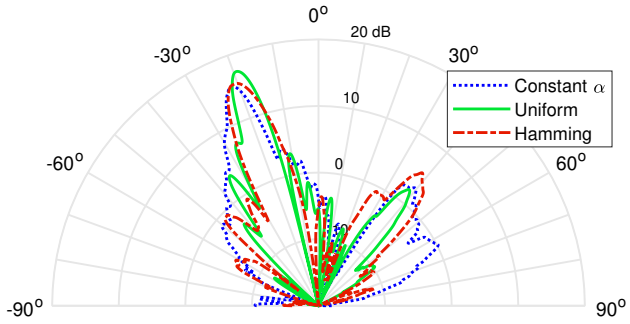

Fig. 13. Measured 2D directivity at 16 GHz for the three aperture distribution cases of Design 2.

representing noisy values when the directivity is not high enough (and secondary lobes start becoming the main one). First, it is noticed that the maximum measured directivity occurs around 16 GHz for all cases, when it was expected at the design frequency of 15 GHz, as is the case in simulation. Therefore, the expected behavior has undergone a systematic frequency shift. Even with this effect, the measured radiation characteristics remain very close to those from simulation. The maximum 2D directivity levels reach their expected values, and their frequency behaviors are very similar to the simulated ones, being almost flat in the corresponding band of interest. In that band, where the BHMS characteristics can be assumed to remain almost constant, the main change is produced in the pointing angle due to the expected frequency scanning. Furthermore, because of this, the measured pointing angle at the shifted frequency is displaced to around $-20°$. The measured 2D directivity diagrams at 16 GHz in Fig. 13 show the different achieved radiation patterns for each case.

Fig. 14 shows a comparison with the simulated directivity patterns at their corresponding peak performance frequency for the three aperture cases. As can be noted, although shifted in frequency, and consequently in angle too, the measured patterns highly resemble those from simulation. Greater sidelobes are noticed with respect to simulations, which is attributed to

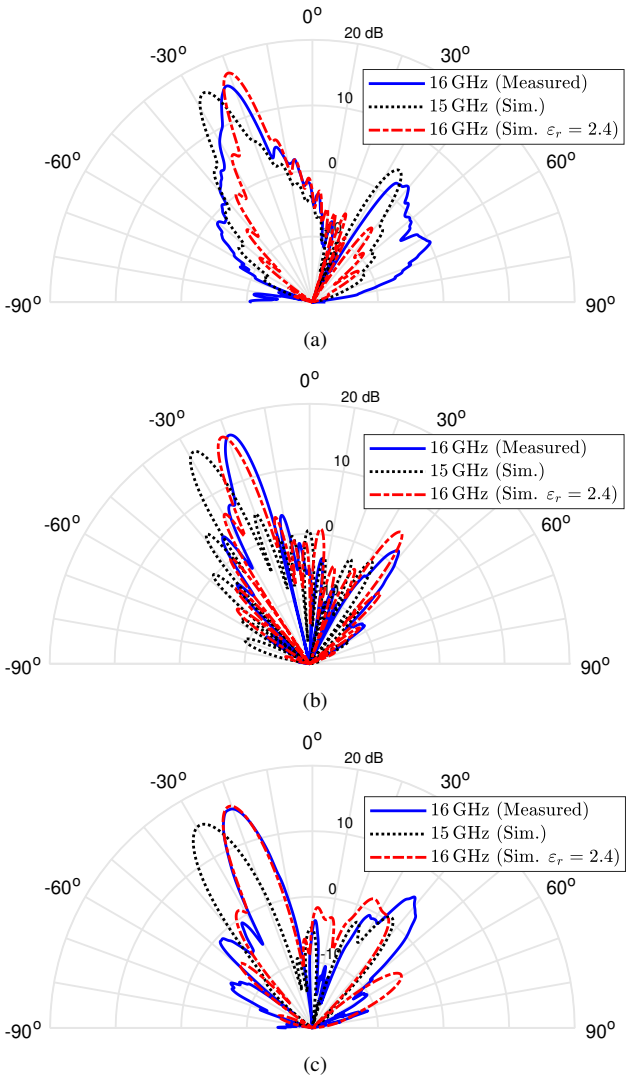

Fig. 14. Measured and simulated 2D directivity patterns at their peak performance frequency for the (a) constant α, (b) Uniform and (c) Hamming aperture distribution cases of Design 2, in addition to the simulated patterns assuming a 20% permittivity deviation.

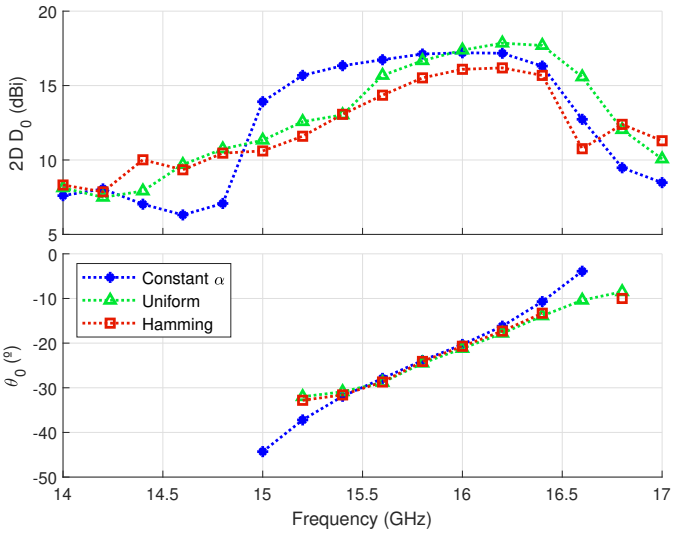

Fig. 15. Simulated maximum 2D directivity (top) and corresponding pointing angle (bottom) for the three aperture cases of Design 2, assuming a 20% permittivity deviation.

the slight behavior degradation expected from the undesired frequency shift. The Hamming aperture case is very sensitive to deviations from the theoretical expectations, as high sidelobe levels defeat its purpose; even so, the experimental result is within simulation expectations, as the sidelobe level around the main lobe is lower than $-15\,\mathrm{dB}$, and the forward spurious lobe was expected. Therefore, simulations and measurements are in very close agreement, except for the frequency shift.

The observed frequency shift is a systematic error, as the $1\,\mathrm{GHz}$ upshift is observed for every measured design. Thus, it is attributed to the BHMS fabrication, as the waveguide alone did have the expected behavior, and the errors from the process of mounting the metasurface into the waveguide would not be systematic. In fact, manually changing the HBMS mounting height did not bring the measurements closer to the predicted results. Thus, after carrying out a qualitative sensitivity study and several experimental tests, it is found that a reasonable source of error that could gracefully shift the frequency behavior without totally degrading the radiation characteristics is a deviation in the metasurface substrate permittivity. In particular, for the observed shift, a downward deviation of around 20% would be required, which would result in $\varepsilon_r = 2.4$. Although this shift is considerably large, it can be treated as a macroscopic averaged error that may arise from other added factors that are difficult to estimate directly, such as copper trace accuracy, layer misalignment, etc. This permittivity deviation would make the unit cells electrically shorter, thus increasing the frequency for which they present the expected electrical length and, consequently, a behavior similar to the nominally designed. This behavior is in close correspondence to the one found in measurements and also in simulations where this permittivity deviation is considered, whose results are also plotted in Fig. 14 for comparison. The simulated patterns that take into account this error are remarkably similar to those from the experiments, both in shape and in the peak performance frequency and pointing angle. The slight discrepancies in pointing angle can be attributed to measurement misalignments. Furthermore, Fig. 15 presents the radiation characteristics with respect to frequency for these modified simulations (again, the pointing angle is only displayed for sufficiently differentiated main beams). Compared to the measured behaviors from Fig. 12, the resemblance is clear for the three designs, observing a highly similar frequency scanning performance, thus validating the hypothesis.

In any case, the relation between the directivity levels of the different aperture cases highly relates to that expected from theory and simulation. This demonstrates that the desired aperture distributions have been achieved and that the operating principle of these aperiodic BHMSs works as expected, demonstrating the concept. In addition, frequency scanning is achieved for frequencies around the peak performance one, as shown in Fig. 16 for the uniform aperture case. The metasurface is able to reasonably maintain the main

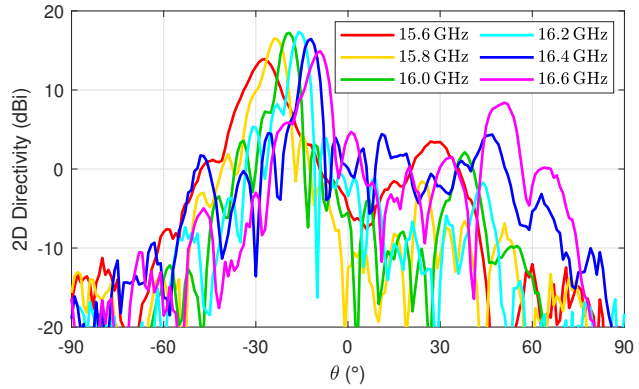

Fig. 16. Measured 2D directivity at different frequencies for the Uniform aperture distribution case of Design 2.

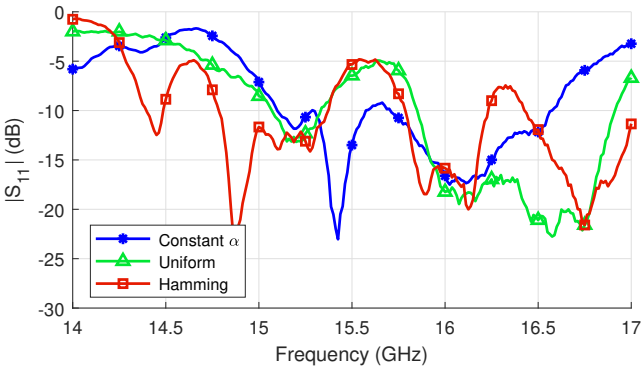

Fig. 17. Measured reflection coefficient for every aperture case of Design 2.

beam shape and directivity level in this band. Note that this occurs even when the suppression of spurious spatial modes is not guaranteed (and higher sidelobes are observed, in consequence) for frequencies different from that the pure transformation is designed for.

The reflection coefficient of these measured prototypes is shown in Fig. 17. The matching at the design frequency of 15 GHz is acceptable, although not great, due to the discussed metasurface fabrication tolerances and the aforementioned deviation in the designed connector location. However, the matching around the shifted frequency of 16 GHz is very good for all cases. This is reasonable as the BHMS works as designed in this band, forcing a single TE mode inside the waveguide to propagate without major reflections, guaranteeing a maximum accepted power. The good matching level is achieved even with the encountered fabrication tolerances, showcasing the resilience of the designs.

VII. Conclusion

A methodology for the design of LWAs with aperture control using bianisotropic Huygens' metasurfaces has been presented. A rigorous theoretical analysis has been followed, and the inclusion of a non-constant leakage factor along the antenna has been made possible through a Slowly Varying Amplitude Approximation approach. This comprises another degree of freedom, in addition to the independent control of the pointing angle or the waveguide height, among others, making the proposed antennas very versatile. The variable leakage factor makes the metasurface physically non-periodic. Therefore, its appropriate radiation can not be simply attributed to an excitation of a given spatial Floquet mode, but to the successful boundary condition implemented by the BHMS.

Several designs with different pointing angles and aperture field distributions have been presented to verify the theoretical derivation. Ideal simulations with impedance conditions have been used to test the used approach, which holds even for very high radiation efficiencies. Then, the microscopic design for the realistic implementation of the unit cells has been assessed. A semi-analytical synthesis algorithm that takes into account the inter-layer coupling has been used. The remarkable similarity between the algorithm-obtained and simulated S-parameters for the synthesized geometries has allowed the avoidance of time-consuming full-wave optimization. Realistic simulations of the complete antennas have been carried out, obtaining a very good agreement with the theoretical predictions, and clearly showing how the field power profile along the antenna aperture behaves as desired.

Finally, several prototypes have been manufactured and measured. A frequency shift with respect to simulations has been observed. Even so, the desired radiation characteristics are achieved, and the predicted relation between different aperture cases is well appreciated, demonstrating the successful control of the variable leakage factor. In addition, good matching is obtained, and the antennas are able to perform frequency scanning in the band around where peak performance is observed. The successful experimental validation of the presented methodology represents a step forward in the efficient design of metasurface-based leaky-wave antennas. By overcoming previous fundamental limitations through a rigorous theoretical formulation, radiation patterns can be engineered, making these antennas more versatile for their use in modern wireless systems.

Appendix
Mathematical Derivation to Obtain the Approximate Dispersion Relation

The dispersion relations in (7) are, in fact, the usual Pythagorean sum of the longitudinal and transverse wavenumbers, with added terms related to their first- and second-order derivatives. Furthermore, the transverse wavenumber (k_y) is responsible for the variation of the longitudinal wavenumber (k_z) along y, hence the partial derivative of the latter can be expressed in terms of the former's, for both regions:

$$\frac{\partial k_z^{\pm}(y)}{\partial y} = \frac{\partial k_z^{\pm}(y)}{\partial k_y^{\pm}(y)} \frac{\partial k_y^{\pm}(y)}{\partial y}. \tag{A.1}$$

Now every differential term in (7) is ensured to be proportional to the derivatives of k_y^- or k_y^+. Moreover, as β^- and β^+ are fixed, and α is imposed to be the same in both regions through the local power conservation condition, then, from (3):

$$\frac{\partial k_y^-(y)}{\partial y} = \frac{\partial k_y^+(y)}{\partial y} = -j\frac{\partial \alpha(y)}{\partial y} \tag{A.2}$$

This way, every differential term in (7) explicitly depends on the value of $\partial\alpha(y)/\partial y$, as:

$$\begin{aligned} k^{-^2} &= k_y^{-^2}(y) + k_z^{-^2}(y) \\ &\quad + (z+d)\cot\left[(z+d)k_z^-(y)\right]\times \\ &\quad \left[2\frac{\partial k_z^-(y)}{\partial k_y^-(y)}k_y^-(y) + 1 + j\frac{\partial}{\partial y}\left(\frac{\partial k_z^-(y)}{\partial k_y^-(y)}\right)\right]\frac{\partial\alpha(y)}{\partial y} \\ &\quad + j(z+d)\cot\left[(z+d)k_z^-(y)\right]\frac{\partial k_z^-(y)}{\partial k_y^-(y)}\frac{\partial^2\alpha(y)}{\partial y^2} \\ &\quad - (z+d)^2\left(\frac{\partial k_z^-(y)}{\partial k_y^-(y)}\right)^2\left(\frac{\partial\alpha(y)}{\partial y}\right)^2, \end{aligned} \tag{A.3}$$

$$\begin{aligned} k^{+^2} &= k_y^{+^2}(y) + k_z^{+^2}(y) \\ &\quad + \left[z\frac{\partial}{\partial y}\left(\frac{\partial k_z^+(y)}{\partial k_y^+(y)}\right) + 1 - j2z\frac{\partial k_z^+(y)}{\partial k_y^+(y)}k_y^+(y)\right]\frac{\partial\alpha(y)}{\partial y} \\ &\quad + z\frac{\partial k_z^+(y)}{\partial k_y^+(y)}\frac{\partial^2\alpha(y)}{\partial y^2} - z^2\left(\frac{\partial\alpha(y)}{\partial y}\right)^2. \end{aligned} \tag{A.4}$$

Thus, assuming a Slowly Varying Amplitude Approximation (SVAA) approach for the value of $\alpha(y)$, its derivative can be neglected. Consequently, all differential terms in (7) can be discarded, resulting in the common, simpler form of the dispersion relation (8), repeated here for convenience:

$$\begin{aligned} k^{-^2} &\simeq k_y^{-^2}(y) + k_z^{-^2}(y), \\ k^{+^2} &\simeq k_y^{+^2}(y) + k_z^{+^2}(y). \end{aligned} \tag{A.5}$$

As $\partial k_z^{\pm}(y)/\partial k_y^{\pm}(y)$ is a recurrent multiplicative factor in (A.3) and (A.4), it is important to ensure that it is not big. Hence, assuming that (A.5) is valid and using (15), then:

$$\frac{\partial k_z^{\pm}(y)}{\partial k_y^{\pm}(y)} = \frac{1}{\sqrt{\left(\frac{k^{\pm}}{k_y^{\pm}}\right)^2 - 1}} \approx \frac{1}{\sqrt{1/\sin^2\theta_{\text{in/out}} - 1}} \tag{A.6}$$

This factor would surpass a value of 10 in the media below (above) the metasurface for θ_{in} (θ_{out}) higher than $85°$, which is not usually practical as it is too extreme. Therefore, this factor would not considerably alter the order of magnitude in (A.1). Consequently, by deduction, the approximate dispersion relation (A.5) remains valid.

REFERENCES

[1] R. C. Hansen, *Phased array antennas*, 2nd ed., ser. Wiley series in microwave and optical engineering. Hoboken, N.J: Wiley, 2009.

[2] A. Hessel, "General characteristics of travelling-wave antennas," in *Antenna Theory*, R. Collin and F. Zucker, Eds. McGraw-Hill, 1969, no. part 2, ch. 19.

[3] A. A. Oliner, "Leaky-wave antennas," in *Antenna Engineering Handbook*, 3rd ed., R. C. Johnson, Ed. Georgia: McGraw-Hill, 1993, ch. 10.

[4] G. B. Wu *et al.*, "Amplitude-modulated leaky-wave antennas," *IEEE Transactions on Antennas and Propagation*, vol. 69, pp. 3664–3676, 7 2021.

[5] A. Araghi, M. Khalily, P. Xiao, and R. Tafazolli, "Holographic-based leaky-wave structures: Transformation of guided waves to leaky waves," *IEEE Microwave Magazine*, vol. 22, pp. 49–63, 6 2021.

[6] O. Quevedo-Teruel *et al.*, "Roadmap on metasurfaces," *Journal of Optics*, vol. 21, no. 7, p. 073002, Jul. 2019.

[7] A. Epstein and G. V. Eleftheriades, "Huygens' metasurfaces via the equivalence principle: design and applications," *J. Opt. Soc. Am. B*, vol. 33, no. 2, pp. A31–A50, Feb 2016.

[8] C. Pfeiffer and A. Grbic, "Metamaterial huygens' surfaces: Tailoring wave fronts with reflectionless sheets," *Phys. Rev. Lett.*, vol. 110, p. 197401, May 2013.

[9] A. Díaz-Rubio and S. A. Tretyakov, "Acoustic metasurfaces for scattering-free anomalous reflection and refraction," *Phys. Rev. B*, vol. 96, p. 125409, Sep 2017.

[10] M. Chen, E. Abdo-Sánchez, A. Epstein, and G. V. Eleftheriades, "Theory, design, and experimental verification of a reflectionless bianisotropic Huygens' metasurface for wide-angle refraction," *Physical Review B*, vol. 97, 3 2018.

[11] A. H. Dorrah, M. Chen, and G. V. Eleftheriades, "Bianisotropic Huygens' metasurface for wideband impedance matching between two dielectric media," *IEEE Transactions on Antennas and Propagation*, vol. 66, pp. 4729–4742, 9 2018.

[12] C. Pfeiffer and A. Grbic, "Controlling vector bessel beams with metasurfaces," *Phys. Rev. Appl.*, vol. 2, p. 044012, Oct 2014.

[13] M. Chen, A. Epstein, and G. V. Eleftheriades, "Design and experimental verification of a passive Huygens' metasurface lens for gain enhancement of frequency-scanning slotted-waveguide antennas," *IEEE Transactions on Antennas and Propagation*, vol. 67, no. 7, pp. 4678–4692, 2019.

[14] T. J. Smy, S. A. Stewart, and S. Gupta, "Surface susceptibility synthesis of metasurface holograms for creating electromagnetic illusions," *IEEE Access*, vol. 8, pp. 93 408–93 425, 2020.

[15] P. Ang, G. Xu, and G. V. Eleftheriades, "Invisibility cloaking with passive and active Huygens's metasurfaces," *Applied Physics Letters*, vol. 118, p. 71903, 2 2021.

[16] C. Pfeiffer and A. Grbic, "Planar lens antennas of subwavelength thickness: Collimating leaky-waves with metasurfaces," *IEEE Transactions on Antennas and Propagation*, vol. 63, no. 7, pp. 3248–3253, 2015.

[17] A. Epstein, J. P. S. Wong, and G. V. Eleftheriades, "Cavity-excited Huygens' metasurface antennas for near-unity aperture illumination efficiency from arbitrarily large apertures," *Nature Communications*, vol. 7, no. 1, p. 10360, Jan. 2016.

[18] G. Minatti *et al.*, "Synthesis of modulated-metasurface antennas with amplitude, phase, and polarization control," *IEEE Transactions on Antennas and Propagation*, vol. 64, pp. 3907–3919, 9 2016.

[19] M. Teniou *et al.*, "Implementation of radiating aperture field distribution using tensorial metasurfaces," *IEEE Transactions on Antennas and Propagation*, vol. 65, pp. 5895–5907, 11 2017.

[20] G. Minatti, E. Martini, and S. Maci, "Efficiency of metasurface antennas," *IEEE Transactions on Antennas and Propagation*, vol. 65, pp. 1532–1541, 4 2017.

[21] M. Faenzi *et al.*, "Metasurface antennas: New models, applications and realizations," *Scientific Reports*, vol. 9, 12 2019.

[22] V. G. Ataloglou and G. V. Eleftheriades, "Arbitrary wave transformations with huygens' metasurfaces through surface-wave optimization," *IEEE Antennas and Wireless Propagation Letters*, vol. 20, no. 9, pp. 1750–1754, 2021.

[23] A. M. Patel and A. Grbic, "A printed leaky-wave antenna based on a sinusoidally-modulated reactance surface," *IEEE Transactions on Antennas and Propagation*, vol. 59, no. 6, pp. 2087–2096, 2011.

[24] B. B. Tierney and A. Grbic, "Controlling leaky waves with 1-d cascaded metasurfaces," *IEEE Transactions on Antennas and Propagation*, vol. 66, pp. 2143–2146, 4 2018.

[25] S. N. Tcvetkova, E. Martini, S. A. Tretyakov, and S. Maci, "Perfect conversion of a TM surface wave into a TM leaky wave by an isotropic periodic metasurface printed on a grounded dielectric slab," *IEEE Transactions on Antennas and Propagation*, vol. 68, pp. 6145–6153, 8 2020.

[26] F. Monticone, N. M. Estakhri, and A. Alù, "Full control of nanoscale optical transmission with a composite metascreen," *Phys. Rev. Lett.*, vol. 110, p. 203903, May 2013.

[27] M. Selvanayagam and G. V. Eleftheriades, "Discontinuous electromagnetic fields using orthogonal electric and magnetic currents for wavefront manipulation," *Opt. Express*, vol. 21, no. 12, pp. 14 409–14 429, Jun 2013.

[28] V. G. Ataloglou, M. Chen, M. Kim, and G. V. Eleftheriades, "Microwave Huygens' metasurfaces: Fundamentals and applications," *IEEE Journal of Microwaves*, vol. 1, no. 1, pp. 374–388, 2021.

[29] S. Tretyakov, *Analytical modeling in applied electromagnetics*, ser. Artech House electromagnetic analysis series. Boston: Artech House, 2003.

[30] E. F. Kuester, M. A. Mohamed, M. Piket-May, and C. L. Holloway, "Averaged transition conditions for electromagnetic fields at a metafilm," *IEEE Transactions on Antennas and Propagation*, vol. 51, pp. 2641–2651, 10 2003.
[31] A. Epstein and G. V. Eleftheriades, "Arbitrary power-conserving field transformations with passive lossless omega-type bianisotropic metasurfaces," *IEEE Transactions on Antennas and Propagation*, vol. 64, no. 9, pp. 3880–3895, 2016.
[32] V. Popov *et al.*, "Omega-bianisotropic metasurface for converting a propagating wave into a surface wave," *Physical Review B*, vol. 100, p. 125103, 9 2019.
[33] A. Mehdipour, J. W. Wong, and G. V. Eleftheriades, "Beam-squinting reduction of leaky-wave antennas using huygens metasurfaces," *IEEE Transactions on Antennas and Propagation*, vol. 63, pp. 978–992, 3 2015.
[34] E. Abdo-Sánchez, M. Chen, A. Epstein, and G. V. Eleftheriades, "A leaky-wave antenna with controlled radiation using a bianisotropic Huygens' metasurface," *IEEE Transactions on Antennas and Propagation*, vol. 67, no. 1, pp. 108–120, 2019.
[35] H. Lee and D. H. Kwon, "Printed metasurface leaky wave antennas based on penetrable aperture field synthesis," *IEEE Transactions on Antennas and Propagation*, vol. 71, pp. 4724–4736, 6 2023.
[36] P. Mateos-Ruiz, V. K. Killamsetty, A. Epstein, and E. Abdo-Sánchez, "Physical implementation of leaky-wave antenna with engineered aperture distribution based on bianisotropic huygens metasurfaces," in *2023 17th European Conference on Antennas and Propagation (EuCAP)*, 2023, pp. 1–5.
[37] Y. Ra'di and S. A. Tretyakov, "Balanced and optimal bianisotropic particles: maximizing power extracted from electromagnetic fields," *New Journal of Physics*, vol. 15, no. 5, p. 053008, may 2013.
[38] M. Selvanayagam and G. V. Eleftheriades, "Circuit Modeling of Huygens Surfaces," *IEEE Antennas and Wireless Propagation Letters*, vol. 12, pp. 1642–1645, 2013.
[39] C. Pfeiffer and A. Grbic, "Bianisotropic metasurfaces for optimal polarization control: Analysis and synthesis," *Phys. Rev. Appl.*, vol. 2, p. 044011, Oct 2014.
[40] G. Xu, S. V. Hum, and G. V. Eleftheriades, "Augmented Huygens' metasurfaces employing baffles for precise control of wave transformations," *IEEE Transactions on Antennas and Propagation*, vol. 67, no. 11, pp. 6935–6946, 2019.
[41] S. Levy, Y. Kerzhner, and A. Epstein, "Rigorous analytical model for metasurface microscopic design with interlayer coupling," in *2019 IEEE International Symposium on Antennas and Propagation and USNC-URSI Radio Science Meeting*, 2019, pp. 195–196.
[42] O. Rabinovich and A. Epstein, "Arbitrary diffraction engineering with multilayered multielement metagratings," *IEEE Transactions on Antennas and Propagation*, vol. 68, no. 3, pp. 1553–1568, 2020.
[43] V. K. Killamsetty and A. Epstein, "Semianalyitcal synthesis scheme for multifunctional metasurfaces on demand," in *2021 Fifteenth International Congress on Artificial Materials for Novel Wave Phenomena (Metamaterials)*, 2021, pp. 123–125.
[44] S. Kuznetsov *et al.*, "Efficient anomalous refraction of thz beams with a multilayer metal–polymer huygens' metasurface," *IEEE Transactions on Terahertz Science and Technology*, vol. 14, no. 1, pp. 109–121, 2024.